Structural, electronic, magnetic, and optical properties of $CuMnInSe_3$ chalcogenide compound

W. Menasri, S. Fetah, and S. Didaoui

Laboratory of materials and renewable energy, Faculty of science, University Pole of M'sila, 28000 M'sila, Algeria.

A. Djerad

Laboratory of Pure and Applied Mathematics, Department of Mathematics, University Pole of Msila, 28000 M'sila, Algeria.

Received 22 november 2023; accepted 13 may 2026

Using density functional theory in conjunction with the FP-LAPW method under the generalized gradient approximation, specifically employing the Perdew 2008 functional GGA-PBEsol, spin-polarized density functional theory computations were conducted to investigate the structural, electronic, and magnetic properties of the quaternary chalcogenide $CuMnInSe_3$ crystal. Both experimental findings and the calculated equilibrium structural parameters exhibit strong concordance. Through an analysis of the spin-polarized band structures and density of states, the half-metallic nature of the studied compound was predicted, characterized by a total magnetic moment of 6 μ_B per unit cell and an energy gap of 0.644 eV. Furthermore, it was observed that the electronic structure is more accurately represented when incorporating the electronic exchange-correlation via the Tran–Blaha modified Becke–Johnson (TB-mBJ) potential, which was employed to precisely compute the band gap of the compound, resulting in an indirect band gap $(X$–$\Gamma)$ of 1.546 eV. Optical properties were predicted by analyzing the spectra of the real and imaginary components of the permittivity, the reflectivity function, and the absorption coefficient. These calculations suggest that this material has potential as an effective ultraviolet sensor.

Keywords: Quaternary chalcogenide; half-metal; magnetic and optical properties; DFT.

DOI: https://doi.org/10.31349/RevMexFis.72.061002

1. Introduction

$CuMnInSe_3$ is an emerging multifunctional semiconductor combining semiconducting and magnetic properties. It belongs to the I–II–III–VI_3 family of chalcogenides, materials well known for their adjustable band gaps, significant spin–orbit coupling, and varied magnetic behavior, which make them promising candidates for spintronics, nonlinear optics, and optoelectronic technologies [1, 2].

The crystal structure of $CuMnInSe_3$ has been experimentally characterized through X-ray powder diffraction analysis [3, 4]. The compound crystallizes in a tetragonal phase that is closely related to the chalcopyrite structure of $CuInSe_2$. In this structure, the symmetry is reduced from the $I\bar{4}2d$ space group to the closely related $P\bar{4}2c$ space group, which is isostructural with $CuFeInSe_3$ and belongs to the sphalerite-derived structural family [5]. Specifically, $CuMnInSe_3$ adopts a chalcopyrite-type tetragonal structure (space group No. 112) with lattice parameters $a = 5.7907$ Å, $c = 11.648$ Å, and $V = 390.58$ Å^3. These values are very similar to those reported for $CuInSe_2$ ($a = 5.781(1)$ Å and $c = 11.642(3)$ Å) [6, 7].

Even though $CuMnInSe_3$ has received considerably less attention than its parent compound $CuInSe_2$, it represents a valuable system for studying diluted magnetic semiconductors and holds potential for future technological applications [8]. While some structural data are available, its electronic and magnetic characteristics are still not well established. This gap provides the basis for the present theoretical study, which seeks to investigate the impact of Mn incorporation on structural stability, electronic behavior, and magnetic properties, in order to better understand its multifunctional character and possible applications.

The paper is organized as follows: Section 2 presents the computational details. The findings and their subsequent analysis are presented in Sec. 3. Finally, Sec. 4 summarizes the main conclusions of this study.

2. Computational details

The present study was performed using first-principles calculations within the framework of density functional theory (DFT), as incorporated in the WIEN2k computational package [9]. The calculations relied on the full-potential linearized augmented plane wave (FP-LAPW) method [10], which constitutes the foundation of the present *ab initio* analysis. The structural properties were thoroughly investigated using the generalized gradient approximation for solids (GGA-PBEsol) [11] to describe exchange–correlation effects, as this functional is recognized for its enhanced accuracy in solid-state systems.

To achieve a more accurate description of the electronic structure, the Tran–Blaha modified Becke–Johnson (TB-mBJ) potential [12] was employed in addition to the

GGA-PBEsol functional. Implemented within the WIEN2k framework, the TB-mBJ potential has been shown to significantly improve the prediction of band gaps in semiconductors and insulators compared with conventional GGA functionals such as PBE or PBEsol, particularly for materials containing localized d- and f-electrons [13]. Consequently, this potential was adopted to obtain a more reliable estimation of the band-gap energy by reducing the well-known underestimation associated with standard GGA approaches, and to provide a more accurate description of the electronic band structure and density of states of $CuMnInSe_3$, which contains a transition metal with partially occupied $3d$ states.

In this approach, the crystal unit cell is divided into non-overlapping muffin-tin (MT) spheres and an interstitial region separating them. The muffin-tin radii (R_{MT}) for Cu, Mn, In, and Se atoms were set to 2.11, 2.11, 1.99, and 2.00 bohr, respectively. The basic functions were partitioned into core and valence states, using an energy cutoff of -6.0 Ry to differentiate between the two regions. The Kohn–Sham equations were solved self-consistently. The core states were treated assuming a spherically symmetric charge density confined within the MT spheres, where only the spherical component of the potential was considered. For the valence states, the potential was expanded in spherical harmonics inside the spheres up to $l_{\max} = 10$. In the interstitial region, the wave functions were represented by plane waves. Brillouin zone integrations [14] were performed using 63 k-points in the irreducible Brillouin zone (IBZ), generated from a $12 \times 12 \times 6$ Monkhorst–Pack grid. Self-consistency was considered achieved when the total energy convergence reached a threshold smaller than 10^{-5} eV.

3. Results and discussion

3.1. Analysis of structural properties

The $CuMnInSe_3$ compound adopts a tetragonal crystal structure belonging to the space group $P\bar{4}2c$ (No. 112) with two formula units per unit cell ($Z = 2$) [3, 4]. The unit cell of the investigated material is illustrated in Fig. 1.

The total energy as a function of unit-cell volume was computed for the non-magnetic (NM), antiferromagnetic (AFM), and ferromagnetic (FM) configurations of $CuMnInSe_3$. The resulting energy–volume data were fitted

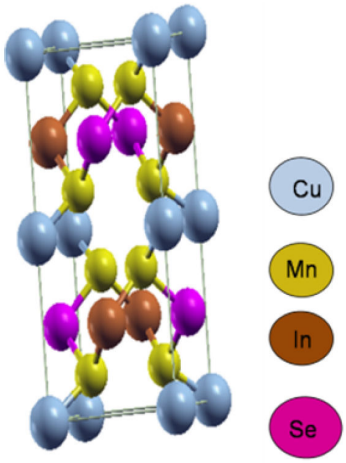


FIGURE 1. Representation of the $CuMnInSe_3$ chalcogenide crystal structure.

to the third-order Birch–Murnaghan equation of state [15], as presented in Fig. 2, to extract the equilibrium structural parameters comprising the equilibrium volume (V_0), the bulk modulus (B), and the pressure derivative (B') of the bulk modulus.

A comparison of the total energies shows that the AFM configuration is more stable than the NM state, whereas the FM configuration possesses the lowest total energy among the considered magnetic arrangements. These results indicate that the ferromagnetic configuration corresponds to the magnetic ground state of the compound. The stabilization of this magnetic state mainly originates from the exchange interactions associated with the Mn $3d$ electrons. Furthermore, the lattice parameters obtained for the FM ground state show excellent agreement with the available experimental data.

The optimized structural parameters, including the relaxed atomic positions, equilibrium lattice constants (a, c, and c/a), equilibrium unit-cell volume (V_0), bulk modulus (B), and pressure derivative (B'), are listed in Table I. The relative deviations between the calculated and experimental lattice constants are less than 1.90% and 3.50% for a and c, respectively, confirming the structural stability of the tetragonal phase. These values are also comparable to those of the parent chalcopyrite compound $CuInSe_2$ [7], indicating that Mn incorporation does not significantly affect the unit-cell volume.

TABLE I. Equilibrium structural parameters: lattice constants a (Å) and c (Å), ratio c/a, equilibrium volume per formula unit V_0 (Å^3), bulk modulus B (GPa), pressure derivative B', and relaxed atomic positions for $CuMnInSe_3$.

	a	c	c/a	V_0	B	B'	Atom	Site	x/a	y/b
$CuMnInSe_3$	5.68	11.24	1.98	362.629	56.375	5.475	Cu	$2c$	0	1/2
	5.7907[a]	11.648[a]	2.01[a]	390.58[a]	–	–	Mn	$2e$	0	0
							In	$2b$	1/2	0
							Se	$8n$	0.2509 (0.227[a])	0.2553 (0.255[a])

[a]Ref. [3]

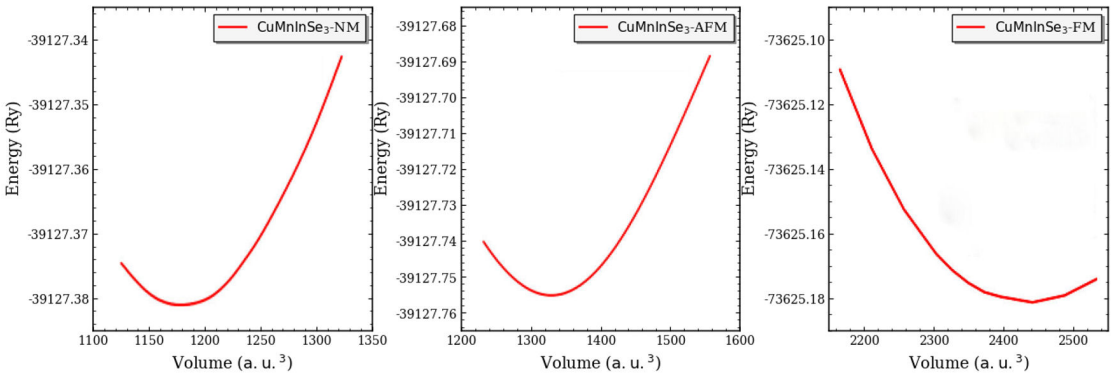


FIGURE 2. Total energy as a function of the unit-cell volume for $CuMnInSe_3$ calculated for different magnetic configurations: non-magnetic (NM), antiferromagnetic (AFM), and ferromagnetic (FM).

To the best of our knowledge, this work provides the first reported estimates of the bulk modulus ($B = 56.375$ GPa) and its pressure derivative ($B' = 5.475$) for $CuMnInSe_3$. The relatively moderate value of B indicates that the material is mechanically soft and exhibits appreciable compressibility, while B' reflects the variation of compressibility under applied pressure.

3.2. Electronic structure and magnetic behavior

The electronic and magnetic characteristics of $CuMnInSe_3$ were analyzed using spin-polarized calculations. The electronic properties of a crystalline material can be assessed through its band structure and density of states (DOS), which together provide detailed insight into its electronic behavior.

Spin-polarized total DOS and band structures were computed using the FP-LAPW method within the GGA-PBEsol and TB-mBJ frameworks, at the optimized equilibrium geometry. The band structures were plotted along the high-symmetry directions of the first Brillouin zone of the tetragonal lattice, separately for majority (spin-up) and minority (spin-down) channels, as shown in Figs. 3 and 4. The asymmetric distribution of spin-up and spin-down states confirms that $CuMnInSe_3$ is not paramagnetic. In the majority-spin channel, several bands cross the Fermi level, resulting in a high DOS and indicating metallic behavior. In contrast, the minority-spin channel exhibits a clear energy gap around the Fermi level, characteristic of semiconducting behavior. This combination confirms the half-metallic character of $CuMnInSe_3$.

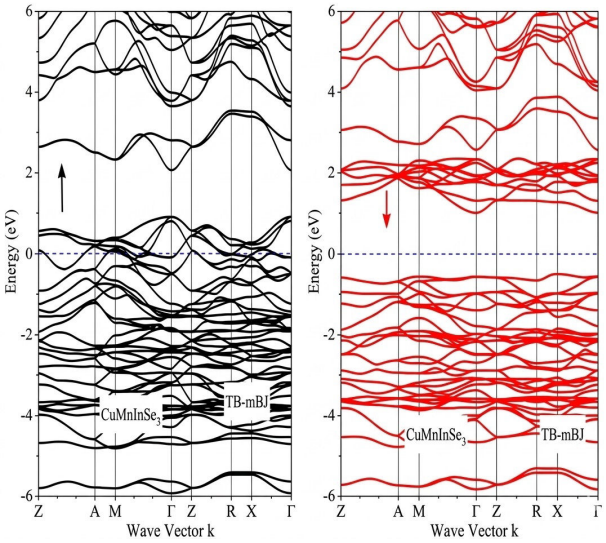


FIGURE 4. Electronic band structure of $CuMnInSe_3$ chalcogenide calculated by TB-mBJ.

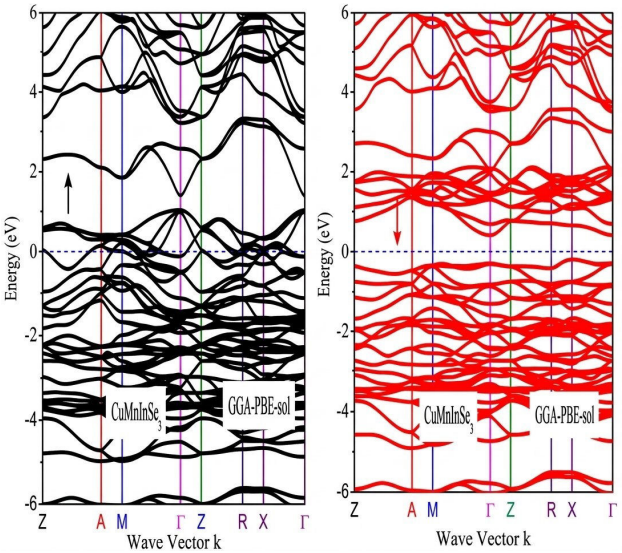


FIGURE 3. Electronic band structure of $CuMnInSe_3$ chalcogenide calculated by GGA-PBEsol.

The spin-resolved partial DOS, illustrated in Fig. 5, further clarifies the elemental contributions near the Fermi level. The $3d$ states of Cu and Mn dominate the top of the valence band for both spin channels, highlighting their crucial role in shaping the electronic properties of $CuMnInSe_3$. Conversely, the $3p$ states of Cu and Se contribute very little in this energy range. In the conduction band, the spin-down $3d$ states of Mn overwhelmingly dominate, with minimal participation from other atomic orbitals.

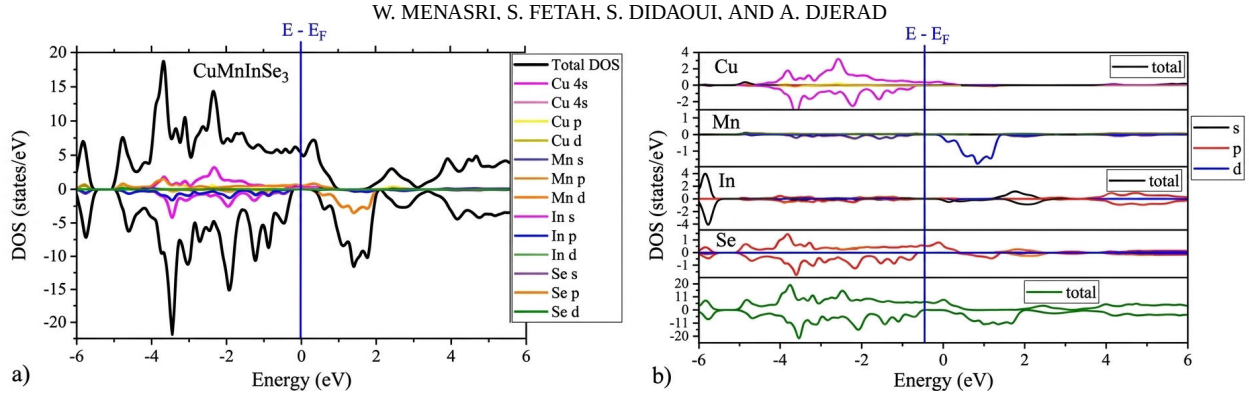


FIGURE 5. Calculated partial and total density of states of $CuMnInSe_3$ chalcogenide obtained by TB-mBJ.

TABLE II. Band gap energy E_g (eV), total and partial magnetic moments (μ_B) for $CuMnInSe_3$ chalcogenide.

	E_g (eV)	μ_{Tot}	μ_{Cu}	μ_{Mn}	μ_{In}	μ_{Se}
GGA-PBEsol	0.644	6.0025	−0.1407	3.18152	0.03756	−0.03756
TB-mBJ	1.546	6.002	−0.2707	3.11252	0.01756	−0.14756

The calculated band gap is indirect, with the valence band maximum located at the M point and the conduction band minimum at the Γ point. While the overall band-structure features obtained from GGA-PBEsol and TB-mBJ functionals are similar, the predicted band-gap values differ significantly, emphasizing the importance of the TB-mBJ potential for accurate band-gap estimation in systems containing transition-metal $3d$ states. Both Cu ($3d^{10}$) and Mn ($3d^5$) atoms have partially filled d-orbitals, which are prone to self-interaction errors in standard DFT. The Tran–Blaha TB-mBJ potential addresses this issue by introducing a semi-local approximation to the exchange potential, better reproducing the derivative discontinuity of the total energy with respect to electron number [12, 16]. For $CuMnInSe_3$, the GGA-PBEsol functional predicts a minority-spin band gap of 0.644 eV, while the inclusion of the mBJ correction increases it to 1.546 eV, bringing it closer to the range observed in related chalcopyrite compounds. The total magnetic moment remains nearly constant at $\sim 6\,\mu_B$ per unit cell, confirming the robustness of the magnetic configuration.

The energy-dependent spin polarization at the Fermi level $P(E_F)$ provides important information about the electronic behavior of a material. For half-metallic systems, $P(E_F)$ reaches unity (100%) [17, 18]. It is defined as

$$P(E_F) = \frac{\rho^{\uparrow}(E_F) - \rho^{\downarrow}(E_F)}{\rho^{\uparrow}(E_F) + \rho^{\downarrow}(E_F)}, \tag{1}$$

where $\rho^{\uparrow}(E_F)$ and $\rho^{\downarrow}(E_F)$ are the total densities of states for spin-up and spin-down electrons at the Fermi level, respectively.

The electrons at the Fermi level are completely spin-polarized (100%), since $\rho^{\downarrow}(E_F) = 0$, as illustrated in Fig. 5, confirming that $CuMnInSe_3$ exhibits half-metallic behavior.

The total magnetic moment (in μ_B) is defined as the difference between the number of occupied spin-up and spin-down states [18]. The atomic magnetic moments of Cu, Mn, In, and Se, along with the total integer magnetic moment μ_{tot} of $CuMnInSe_3$, were calculated using both the TB-mBJ and GGA-PBEsol methods and are summarized in Table II. Our results yield a total spin magnetic moment of $6\,\mu_B$ per unit cell from both computational approaches, satisfying the requirement for half-metallic materials [17]. Specifically, the Mn atom exhibits a magnetic moment of approximately $3.182\,\mu_B$ within GGA-PBEsol and $3.113\,\mu_B$ using the TB-mBJ approach. In contrast, Cu and Se atoms display small negative magnetic moments, while In atoms contribute only a very weak magnetic moment.

3.3. Optical properties and analysis

The optical properties of a solid describe the response of a material to incident electromagnetic radiation, leading to polarization effects and the excitation of conduction electrons. The interaction between photons and the electronic structure results in energy loss and charge polarization, constituting the optical response of the system. This can be described by the complex dielectric function

$$\varepsilon_{\alpha\beta}(\omega) = \varepsilon_1^{\alpha\beta}(\omega) + i\,\varepsilon_2^{\alpha\beta}(\omega), \quad \alpha,\beta = x,y,z. \tag{2}$$

The crystal symmetry of the compound implies the following relations for the dielectric tensor components:

$$\varepsilon_i^{xx}(\omega) = \varepsilon_i^{yy}(\omega) \equiv \varepsilon_i^{\parallel}(\omega), \qquad \varepsilon_i^{zz}(\omega) \equiv \varepsilon_i^{\perp}(\omega). \tag{3}$$

TABLE III. Energy ranges for the real part $\varepsilon_1^{xx(zz)}$ of the dielectric function.

	$\varepsilon_1 < 0$ (eV)	$\varepsilon_1 > 0$ (eV)	$\varepsilon_1 = 0$ (eV)
$E \parallel xx$	0.48-0.942, > 8.50	0.942-8.50	0.48, 0.942, 8.50
$E \parallel zz$	0.60-1.15, > 8.50	1.15-8.50	0.48, 0.942, 8.50

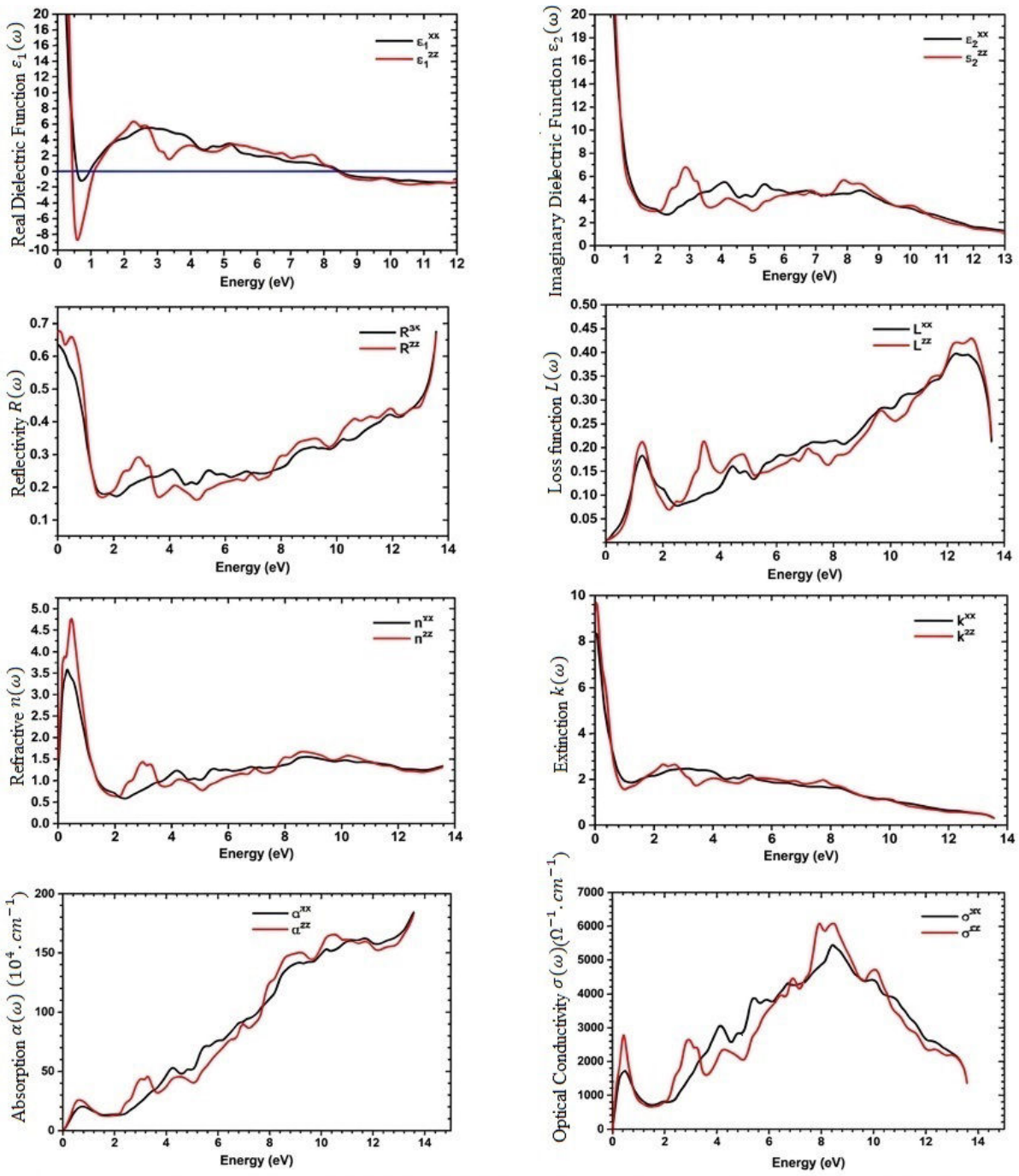


FIGURE 6. Variation of the optical parameters as a function of absorption energy for CuMnInSe$_3$ chalcogenide.

The calculated optical spectra are not identical along the xx and zz directions, indicating optical anisotropy in the compound. Figure 6 shows the variation of the optical parameters as a function of photon energy.

The real part $\varepsilon_1^{xx(zz)}(\omega)$ takes large positive values at low photon energies, reflecting strong electronic polarizability. As the photon energy increases, it gradually decreases. Negative values of $\varepsilon_1^{xx(zz)}$ indicate that electromagnetic waves cannot propagate inside the material in this energy region, resulting in strong reflection and absorption. The photon energies at which $\varepsilon_1^{xx(zz)}$ crosses zero correspond to plasma resonance frequencies. The energy ranges for the sign of the real part are summarized in Table III.

The imaginary part $\varepsilon_2^{xx(zz)}(\omega)$ describes absorption processes arising from interband electronic transitions. In the low-energy region (below $\approx$ 0.85 eV), the finite value of $\varepsilon_2^{xx(zz)}$ indicates the presence of free carriers, characteristic of metallic-like behavior. At higher photon energies, several

TABLE IV. Refractive index values $n_{xx(zz)}(0)$ and energies at which $n_{xx(zz)} = 1$.

$n_{xx}(0)$	$n_{zz}(0)$	$E(n_{xx} = 1)$ (eV)	$E(n_{zz} = 1)$ (eV)
1.26	1.59	1.42, 3.45	1.42, 2.75, 3.45, 5.63

pronounced peaks appear due to enhanced interband transitions. The main peaks are located at approximately 1.92 (2.84) eV, 4.08 (4.26) eV, 5.43 (6.89) eV, and 8.33 (8.02) eV for the xx and zz polarizations, respectively, corresponding to electronic transitions mainly in the visible and ultraviolet energy regions.

The most prominent peaks in the electronic energy loss spectrum occur in the ultraviolet region. The main peaks of $L_{xx}(\omega)$ and $L_{zz}(\omega)$ appear at 12.76 eV and 12.79 eV, respectively. Owing to the metallic nature of the compound, the reflectivity at zero frequency is relatively high, with $R_{xx}(0) = 62\%$ and $R_{zz}(0) = 68\%$ in the infrared region. In the visible range, the reflectivity reaches about 25% and 28% at photon energies of 4.14 eV and 2.91 eV for the xx and zz directions, respectively. A strong reflection of approximately 65% at 13.54 eV in the ultraviolet region further confirms the metallic behavior and the absence of optical transparency.

The extinction coefficient $K(\omega)$ decreases significantly with increasing photon energy in the visible region and above 5.00 eV, whereas the refractive indices n_{xx} and n_{zz} increase and reach their maximum values at 0.29 eV and 0.45 eV, respectively (Table IV).

Consistent with this metallic behavior, the absorption coefficient starts at very low photon energies and increases rapidly across the visible and ultraviolet regions. The absorption spectrum reaches saturation around 8.47 eV, coinciding with the maximum in the optical conductivity spectrum. Overall, the calculated dielectric function, energy-loss spectrum, reflectivity, refractive indices, extinction coefficient, and absorption coefficient consistently indicate a metallic character, anisotropic optical response, and strong ultraviolet absorption of the compound.

4. Conclusion

The structural, electronic, optical, and magnetic properties of the novel half-metal chalcogenide quaternary compound $CuMnInSe_3$ have been investigated using first-principles calculations. The computed structural parameters were found to be in good agreement with available experimental data. The half-metallic nature of the material was confirmed through analysis of the spin-polarized band structures: the majority-spin channel shows metallic behavior while the minority-spin channel exhibits a semiconducting indirect band gap of 0.644 eV and 1.546 eV within the GGA-PBEsol and TB-mBJ approximations, respectively. A total magnetic moment of $6\,\mu_{\rm B}$ was obtained from both computational approaches. Additionally, strong absorption in the visible and ultraviolet regions was observed, suggesting that the compound could serve as an effective UV sensor or far-ultraviolet photodetector.

1. S. A. Chambers and Y. K. Yoo, New materials for spintronics, *MRS Bull.* **28** (2003) 706, https://doi.org/10.1557/mrs2003.210
2. G. A. Medvedkin *et al.*, Novel spintronic materials based on ferromagnetic semiconductor chalcopyrites, *Int. J. Nanosci.* **3** (2004) 39, https://doi.org/10.1142/S0219581X04001791
3. G. E. Delgado, J. A. Flores-Cruz, P. Grima-Gallardo, M. Quintero, and A. Moreno, Synthesis and crystal structure of three new quaternary compounds in the system Cu–Mn–III–Se_3 (III = Al, Ga, In), *Mater. Res.* **21** (2018) e20160748, https://doi.org/10.1590/1980-5373-MR-2016-0748
4. G. E. Delgado, P. Grima-Gallardo, M. Quintero, and C. Chacón, Preparation and structural characterization of the new diamond-like semiconductor $CuMnInSe_3$, *Rev. Téc. Fac. Ing. Univ. Zulia* **41** (2018) 25.
5. A. J. Mora, G. E. Delgado, and P. Grima-Gallardo, Crystal structure of $CuFeInSe_3$ from X-ray powder diffraction data, *Phys. Status Solidi A* **204** (2007) 547, https://doi.org/10.1002/pssa.200622395
6. S. Chen, X. G. Gong, A. Walsh, and S.-H. Wei, Electronic structure and stability of quaternary chalcogenide semiconductors derived from cation cross-substitution of II-VI and I-III-VI_2 compounds, *Phys. Rev. B* **79** (2009) 165211, https://doi.org/10.1103/PhysRevB.79.165211
7. K. S. Knight, The crystal structures of $CuInSe_2$ and $CuInTe_2$, *Mater. Res. Bull.* **27** (1992) 161, https://doi.org/10.1016/0025-5408(92)90209-I
8. Y.-J. Zhao and A. Zunger, Electronic structure and ferromagnetism of Mn-substituted $CuAlS_2$, $CuGaS_2$, $CuInS_2$, $CuGaSe_2$, and $CuGaTe_2$, *Phys. Rev. B* **69** (2004) 104422, https://doi.org/10.1103/PhysRevB.69.104422
9. K. Schwarz, P. Blaha, and G. K. H. Madsen, Electronic structure calculations of solids using the WIEN2k package for material sciences, *Comput. Phys. Commun.* **147** (2002) 71, https://doi.org/10.1016/S0010-4655(02)00206-0
10. P. Blaha, K. Schwarz, P. Sorantin, and S. B. Trickey, Full-potential, linearized augmented plane wave programs for crystalline systems, *Comput. Phys. Commun.* **59** (1990) 399, https://doi.org/10.1016/0010-4655(90)90187-6
11. J. P. Perdew *et al.*, Restoring the density-gradient expansion for exchange in solids and surfaces, *Phys. Rev. Lett.* **100** (2008) 136406, https://doi.org/10.1103/PhysRevLett.100.136406

12. F. Tran and P. Blaha, Accurate band gaps of semiconductors and insulators with a semilocal exchange-correlation potential, *Phys. Rev. Lett.* **102** (2009) 226401, https://doi.org/10.1103/PhysRevLett.102.226401

13. D. Koller, F. Tran, and P. Blaha, Merits and limits of the modified Becke–Johnson exchange potential, *Phys. Rev. B* **83** (2011) 195134, https://doi.org/10.1103/PhysRevB.83.195134

14. P. E. Blöchl, O. Jepsen, and O. K. Andersen, Improved tetrahedron method for Brillouin-zone integrations, *Phys. Rev. B* **49** (1994) 16223, https://doi.org/10.1103/PhysRevB.49.16223

15. F. D. Murnaghan, The compressibility of media under extreme pressures, *Proc. Natl. Acad. Sci.* **30** (1944) 244, https://doi.org/10.1073/pnas.30.9.244

16. D. Koller, F. Tran, and P. Blaha, Improving the modified Becke–Johnson exchange potential, *Phys. Rev. B* **85** (2012) 155109, https://doi.org/10.1103/PhysRevB.85.155109

17. I. Galanakis, P. H. Dederichs, and N. Papanikolaou, Slater–Pauling behavior and origin of the half-metallicity of the full-Heusler alloys, *Phys. Rev. B* **66** (2002) 174429, https://doi.org/10.1103/PhysRevB.66.174429

18. I. I. Mazin, How to define and calculate the degree of spin polarization in ferromagnets, *Phys. Rev. Lett.* **83** (1999) 1427. https://doi.org/10.1103/PhysRevLett.83.1427